CHIN. PHYS. LETT. Vol. 38, No. 7 (2021) 070303

Entirety of Quantum Uncertainty and Its Experimental Verification

Jie Xie(谢杰)[1,2†], Li Zhou(周立)[3†], Aonan Zhang(张傲男)[1,2], Huichao Xu(徐慧超)[1,2], Man-Hong Yung(翁文康)[4,5], Ping Xu(徐平)[1,2,6], Nengkun Yu(俞能昆)[7*], and Lijian Zhang(张利剑)[1,2*]

[1]*National Laboratory of Solid State Microstructures, College of Engineering and Applied Sciences and School of Physics, Nanjing University, Nanjing 210093, China*
[2]*Collaborative Innovation Center of Advanced Microstructures, Nanjing University, Nanjing 210093, China*
[3]*Department of Computer Science and Technology, Tsinghua University, Beijing 100084, China*
[4]*Shenzhen Institute for Quantum Science and Engineering and Department of Physics, Southern University of Science and Technology, Shenzhen 518055, China*
[5]*Shenzhen Key Laboratory of Quantum Science and Engineering, Southern University of Science and Technology, Shenzhen 518055, China*
[6]*Institute for Quantum Information & State Key Laboratory of High Performance Computing, College of Computer, National University of Defense Technology, Changsha 410073, China*
[7]*Centre for Quantum Software and Information, School of Software, Faculty of Engineering and Information Technology, University of Technology Sydney, NSW, Australia*

(Received 7 March 2021; accepted 5 June 2021; published online 21 June 2021)

As a foundation of quantum physics, uncertainty relations describe ultimate limit for the measurement uncertainty of incompatible observables. Traditionally, uncertainty relations are formulated by mathematical bounds for a specific state. Here we present a method for geometrically characterizing uncertainty relations as an entire area of variances of the observables, ranging over all possible input states. We find that for the pair of position and momentum operators, Heisenberg's uncertainty principle points exactly to the attainable area of the variances of position and momentum. Moreover, for finite-dimensional systems, we prove that the corresponding area is necessarily semialgebraic; in other words, this set can be represented via finite polynomial equations and inequalities, or any finite union of such sets. In particular, we give the analytical characterization of the areas of variances of (a) a pair of one-qubit observables and (b) a pair of projective observables for arbitrary dimension, and give the first experimental observation of such areas in a photonic system.

DOI: 10.1088/0256-307X/38/7/070303

Quantum mechanics is revolutionizing our outlook on the world. The most dramatic change may be "god does play dice with the universe". In other words, quantum world is unpredictable inherently. Heisenberg's uncertainty principle is the most famous result of this unpredictability of the quantum world.[1] Roughly speaking, it asserts a fundamental limit to the precision with which the position and momentum can be known simultaneously. After that, many efforts have been devoted to understand this mystery. Recent years, the uncertainty relation still aroused a lot of research interests and shows more and more applications in quantum information science, such as providing separability criteria,[2–5] determining nonlocality[6] and device-independent quantum cryptography.[7] Many types of uncertainty relations have been proposed[8,9] and aroused a heated discussion, especially the error-disturbance relations on the joint measurement of two incompatible observables.[10–13]

The most well-known uncertainty relation of position x and momentum p was rigorously proven by Kennard[14] and Weyl,[15] $\Delta^2 x\,\Delta^2 p \geq \hbar^2/4$, where $\Delta^2 x$ and $\Delta^2 p$ stand for the variances of x and p, e.g., $\Delta^2 x = \langle x^2\rangle - \langle x\rangle^2$. Then Robertson[16] extended it for two arbitrary observables A and B, $\Delta^2 A\,\Delta^2 B \geq |\langle [A,B]\rangle|^2/4$, where $\langle [A,B]\rangle$ stands for the ensemble average of the commutator $[A,B]$ with respect to a specific state. Later, this inequality was improved by Schrödinger.[17] Whereas, all the above-mentioned uncertainty relations deal with the product of variances of quantum observables, which can be trivial when one of the variances goes to zero,[18] e.g., if the system is in an eigenstate of A, then $\Delta^2 A = 0$. Due to this problem, uncertainty relations in the form

Supported by the National Key Research and Development Program of China (Grant No. 2017YFA0303703), the National Natural Science Foundation of China (Grant Nos. 91836303, 61975077, 61490711, 11690032, 11875160, and U1801661), the Natural Science Foundation of Guangdong Province (Grant No. 2017B030308003), the Key R&D Program of Guangdong Province (Grant No. 2018B030326001), the Science, Technology and Innovation Commission of Shenzhen Municipality (Grant Nos. JCYJ20170412152620376, JCYJ20170817105046702, and KYTDPT20181011104202253), the Economy, Trade and Information Commission of Shenzhen Municipality (Grant No. 201901161512), Guangdong Provincial Key Laboratory (Grant No. 2019B121203002), ARC DECRA 180100156 and ARC DP210102449.
†These authors contributed equally to this work.
*Corresponding authors. Email: nengkunyu@gmail.com; lijian.zhang@nju.edu.cn
© 2021 Chinese Physical Society and IOP Publishing Ltd

of summation of variances of observables have been proposed.[18−24] Moreover, some researchers think that entropy would be the more natural and reasonable way to characterize uncertainty.[25−32] However, these uncertainty relations do not give an overall description for all quantum states, in the sense that they either give a state-dependent[16,18,19,21−23] bound or a state-independent lower bound revealing limited information.[20,28,30,33−35]

To give an universal description of the quantum uncertainty for all states, the concept of uncertainty region (UR) has been proposed. It is the set of variances $\{(\Delta^2 O_1, \ldots, \Delta^2 O_n)\}$ (given the broad interests and tremendous studies on variance-based uncertainty relations,[11,34,36] here we mainly focus on the variance as uncertainty measure) of a set of observables $\{O_1, \ldots, O_n\}$ for all quantum states, naturally forming a geometric area in Euclidean space, from which different uncertainty relations, no matter in the product or summation form, can be obtained. The attempt to derive lower bound of certain uncertainty relation with UR-based method can date back as early as 1998.[29] Recent years, variance-based uncertainty regions for a pair of and any number of traceless qubit observables were obtained as state-independent uncertainty relations in Refs. [37,38], both of which can be as consequences of the results in the earlier papers.[7,33] After that, nontrivial URs of some specific pairs of qutrit observables were also given,[39] while URs of a pair of arbitrary qutrit observables or higher-dimensional nontrivial quantum observables are very difficult to derive, because the quantum state space becomes very complicated as the dimension grows. Recently, algorithms for numerically calculating the URs have been investigated.[34] In addition, the authors of Ref. [34] also showed the application of UR in detecting entanglement in noisy systems and it has been experimentally demonstrated in a two-qutrit photonic system.[36]

In this work, we first propose the concept of UR for pure states and mixed states, and show that both uncertainty regions are semialgebraic sets in a Euclidean space. We characterize the URs of a pair of projective operators, which show the same results as those of Pauli observables and can be easily extended to arbitrary quantum observables in the qubit case. For an infinite-dimensional system, we show that the standard Heisenberg's uncertainty principle represents the exact UR of x and p. For a finite-dimensional system, we give the analytical characterization of URs of a pair of arbitrary qubit and qudit projectors. In addition, we give the first experimental observation of quantum URs for qubit and qutrit projective measurements with photonic setups. Our experimental results show good agreement with the theoretical prediction.

Theory. For a set of observables $\{O_1, \ldots, O_n\}$, finite or infinite-dimensional, we are interested in the following two URs, $R_p := \{(\Delta^2 O_{1,\psi}, \ldots, \Delta^2 O_{n,\psi}) : \langle\psi|\psi\rangle = 1\}$ and $R_m := \{(\Delta^2 O_{1,\rho}, \ldots, \Delta^2 O_{n,\rho}) : \rho \geq 0, \mathrm{Tr}\rho = 1\}$, namely the URs for pure states and mixed states, where $\Delta^2 O_{i,\psi} = \langle\psi|O_i^2|\psi\rangle - \langle\psi|O_i|\psi\rangle^2$ and $\Delta^2 O_{i,\rho} = \mathrm{Tr}({O_i}^2\rho) - \mathrm{Tr}^2(O_i\rho)$, denoting the variance of O_i. It is obvious that $R_p \subset R_m$, besides this, we have the following characterization.

Theorem 1: In finite-dimensional Hilbert space with dimension d, R_m and R_p are both semialgebraic sets.

Proof: A semialgebraic set in $\mathbb{R}^n$ is defined by the finite union of the sets determined by a finite number of polynomial equations $p(x_1, \ldots, x_n) = 0$ and inequalities $q(x_1, \ldots, x_n) > 0$. We can parameterize ρ using $d^2 - 1$ real parameters $x_1, \ldots, x_{d^2-1}$, then observe that

$$S_m := \{(\Delta^2 O_{1,\rho}, \ldots, \Delta^2 O_{n,\rho}, x_1, \ldots, x_{d^2-1}) : \rho \sim (x_1, \ldots, x_{d^2-1})\}$$

is semialgebraic. One of the most important property of semialgebraic sets, known as the Tarski–Seidenberg theorem,[40] is that they are closed under the projection operators: that is, projecting a semialgebraic set onto a linear subspace yields another semialgebraic set. Therefore, R_m is semialgebraic. The same idea shows that R_p is semialgebraic where only $2d - 1$ real parameters are used.

Furthermore, when considering the UR of two projective operators, we have the following conclusion.

Theorem 2: For two projectors P and Q, we can always have

$$R_p = R_m.$$

That is, mixed states will not generate extra uncertainty regions rather than pure states. However, this is not generally true when more projectors involved and we leave the proof of this theorem in the Supplemental Material, Section I(A).

For infinite-dimensional system, we are interested in the joint distribution of $\Delta^2 x$ and $\Delta^2 p$. Here, we only consider the wave packet for free particles (Generally, the physical system may be complex and it is not easy to characterize the exact uncertainty region).

Theorem 3: For one-dimensional free particles, two uncertainty regions for pure states and mixed states are the same:

$$R_p = R_m = \left\{(x, y) : xy \geq \frac{\hbar}{2}, x, y > 0\right\}.$$

The proof of this theorem is completed by considering the one-dimensional Gaussian wave packet, see more details in the Supplemental Material, Section I(B).

Next, we start to give the analytical characterization of the areas of UR for a pair of projective operators. Before that, we introduce the following famous Jordan's lemma[41] used in the characterization.

Lemma 1: Let P and Q are two projective operators in $\mathbb{C}^d$. Then there exists a basis of $\mathbb{C}^d$ in which P and Q are simultaneously block diagonal, with l blocks

of size one or two such that either (for one-dimensional blocks)

$$P_i, Q_i \in \{(0), (1)\},$$

or (for two-dimensional blocks)

$$P_i = \begin{pmatrix} 1 & 0 \\ 0 & 0 \end{pmatrix}, \ Q_i = \begin{pmatrix} \cos^2\theta_i & \cos\theta_i \sin\theta_i \\ \cos\theta_i \sin\theta_i & \sin^2\theta_i \end{pmatrix} \quad (1)$$

with $\theta_1, \ldots, \theta_l \in (0, \frac{\pi}{2}]$.

For the qubit system, we only need to care about rank-1 projectors, whose UR is relatively easy to derive and based on the results of rank-1 projectors, URs for a pair of arbitrary Hermitian observables can be consequently obtained, as will show in the following. For higher-dimensional systems, using this lemma and the qubit's results, we compute the R_m and R_p of two projective observables with arbitrary dimension. For the convenience of the following clarification, we denote the d-dimensional URs of two projective observables as $R^{(d)}$, and $R_p^{(d)}$ or $R_m^{(d)}$ for pure or mixed states, respectively.

Without loss of generality, we consider two-trace one-qubit projectors A and B written in the Bloch representation that $A = (I + \boldsymbol{a}\cdot\boldsymbol{\sigma})/2, B = (I + \boldsymbol{b}\cdot\boldsymbol{\sigma})/2$, where $\boldsymbol{a} = (a_x, a_y, a_z), \boldsymbol{b} = (b_x, b_y, b_z)$ are qubit Bloch vectors and $\boldsymbol{\sigma} = \sigma_x \boldsymbol{i} + \sigma_y \boldsymbol{j} + \sigma_z \boldsymbol{k}$ is the Pauli operator vector. Since $R_m = R_p$, we only consider an arbitrary density matrix $\rho = (I + \boldsymbol{r}\cdot\boldsymbol{\sigma})/2$ with Bloch vector $\boldsymbol{r} = (r_x, r_y, r_z)$. According to Lemma 1, $\boldsymbol{a}$ and $\boldsymbol{b}$ can always be written in a basis such that $\boldsymbol{a} = (0, 0, 1)$ and $\boldsymbol{b} = [\sin(2\theta), 0, \cos(2\theta)]$, so that A, B have the exact form of P_i, Q_i in Eq. (1) and we define $\Theta(A, B) = \theta$ as the angle between two projectors A and B in such basis. It is this angle that uniquely determines the shape of $R^{(2)}$ (the same for qudit). For two known projectors, the only constraint that restricts the obtainable region of $(\Delta^2 A, \Delta^2 B)$ is that $r^2 \leq 1$ ($\boldsymbol{r}$ should represent a physical state with positive semi-definite density matrix). Thus by this constraint, $R^{(2)}$ can be derived as the union set of the following two regions [see the details of derivation in Supplemental Material, Section I(C)]

$$R_1^{(2)}: \begin{cases} \Delta^2 A + \Delta^2 B \geq [1 + \cos^2(2\theta)]/4, \\ \Delta^2 A, \Delta^2 B \leq 1/4, \end{cases} \quad (2)$$

$$R_2^{(2)}: \begin{cases} \Delta^2 A + \Delta^2 B \leq [1 + \cos^2(2\theta)]/4, \\ [16x_1^2/\cos^2(2\theta)] + [16y_1^2/\sin^2(2\theta)] \leq 1, \end{cases} \quad (3)$$

where x_1 and y_1 are

$$\begin{pmatrix} x_1 \\ y_1 \end{pmatrix} = \sqrt{2} \begin{pmatrix} \cos\frac{\pi}{4} & \sin\frac{\pi}{4} \\ -\sin\frac{\pi}{4} & \cos\frac{\pi}{4} \end{pmatrix} \begin{pmatrix} \Delta^2 A - \frac{1}{8} \\ \Delta^2 B - \frac{1}{8} \end{pmatrix}.$$

It can be seen that $R_1^{(2)}$ represents a right triangle on the upper right corner of the region and $R_2^{(2)}$ is part of a tilted ellipse centered at $(1/8, 1/8)$ next to $R_1^{(2)}$, as shown in Fig. 1(a). The long axis of the ellipse is proportional to $|\cos(2\theta)|$ and the minor axis is proportional to $|\sin(2\theta)|$.

Points on the boundary of this ellipse can be achieved by states on the equatorial plane of the Bloch ball satisfying $r_x^2 + r_z^2 = 1$ [see the Supplemental Material, Section I(C)]. We call these states the "boundary states" or "real states", which generate most of the boundary points of $R^{(2)}$. It is obvious that when the angle between the two projectors is $\Theta = 0$, we have $A = B$ and $R^{(2)}$ becomes a line $\Delta^2 A = \Delta^2 B$. As θ grows larger, the long axis (on the line $\Delta^2 A = \Delta^2 B$) of ellipse shrinks while the minor axis gets longer. When $\theta = \pi/4$, the original long axis becomes 0 and the ellipse becomes a line equaling to its minor axis, as depicted in Fig. 1(a). From the $R^{(2)}$, it can also be identified that, in this situation, A and B achieve maximum uncertainty in the summation form at $\theta = \pi/4$, $\Delta^2 A + \Delta^2 B \geq \frac{1}{4}$. This gives the intuition that we can direct define the geometric features of UR as a measure of incompatibility of two observables, for example, in this situation the length of the ellipse's axis.

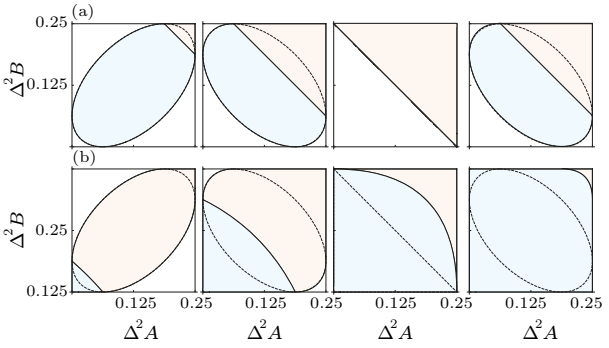

Fig. 1. Theoretical characterization of uncertainty regions. Uncertainty regions of a pair of (a) qubit and (b) qutrit projective observables with different angles $\Theta = \pi/12, \pi/6, \pi/4, \pi/3$ (from left to right). R_1 and R_2 are filled with light yellow and light blue colors, respectively. The dashed curves represent the ellipses given by the second inequality in Eq. (3).

As mentioned above, in the qubit case, this characterization is not limited to projective observables. For any Hermitian observable O_i, there exists a $\lambda_i \in \mathbb{R}$ such that $O_i - \lambda_i I$ is rank 1. Therefore, the UR of two Hermitian observables O_1, O_2 can be characterized by transforming them into two projective observables $O_1 - \lambda_1 I$ and $O_2 - \lambda_2 I$, which share the same UR up to some scalings.

With the above results of $R^{(2)}$ for qubit projectors and applying Lemma 1, the problem of finding $R^{(d)} (d \geq 3)$ can be reduced into qubit subspace of higher-dimensional systems. More specifically, we can always find a basis in which arbitrary two rank-1 projective operators can be written as

$$A = \begin{pmatrix} 1 & 0 & \\ 0 & 0 & \\ & & \ddots \end{pmatrix}, \ B = \begin{pmatrix} \cos^2\theta & \cos\theta\sin\theta & \\ \cos\theta\sin\theta & \sin^2\theta & \\ & & \ddots \end{pmatrix}, \quad (4)$$

where all the blank spaces are equal to 0, which indicate that the two observables are reduced to a qubit subspace. Thus the density matrix ρ can also be equivalently written in the qubit subspace, by setting all the matrix elements equal to 0 apart from the 2×2 block in the left upper corner, i.e.,

$$\rho = \begin{pmatrix} \rho^{(2)} & & \\ & \ddots & \end{pmatrix}. \tag{5}$$

Here $\rho^{(2)}$ is the nonzero 2×2 block representing an unnormalized qubit density matrix, for $\rho^{(2)}$ no longer satisfies the trace one requirement but still needs to be positive. Therefore, we can write $\rho^{(2)}$ as

$$\rho^{(2)} = \frac{1}{2}(\alpha I + \boldsymbol{r} \cdot \boldsymbol{\sigma}), \quad r^2 = 1$$

with $0 \leq \alpha \leq 1$, and the positivity of $\rho^{(2)}$ suggests $r^2 \leq \alpha^2$. Here $\alpha = \mathrm{Tr}[\rho^{(2)}]$ is the probability with ρ being projected onto the qubit subspace. From the above statements in Eqs. (4) and (5), it is obvious that all the calculations can be reduced in the qubit subspace. The only difference is that the density matrix $\rho^{(2)}$ becomes an unnormalized one. Similar to the qubit case, using the constraint $r^2 \leq \alpha^2$, we can derive the following two regions that form $R^{(d)}$ $(d \geq 3)$ (see the Supplemental Material, Section I(D) for more details),

$$R_1^{(d)}: \begin{cases} 4(\Delta^2 A + \Delta^2 B) \pm 2\cos(2\theta)(1 - 4\Delta^2 A)^{1/2} \\ \times (1 - 4\Delta^2 B)^{1/2} \geq (1 + \cos^2 2\theta), \\ \sqrt{1 - 4\Delta^2 A} + \sqrt{1 - 4\Delta^2 B} \leq 2\cos^2\theta, \end{cases} \tag{6}$$

$$R_2^{(d)}: \sqrt{1 - 4\Delta^2 A} + \sqrt{1 - 4\Delta^2 B} \geq 2\cos^2\theta. \tag{7}$$

The second inequality in Eq. (6) gives the exact region of $R^{(2)}$ and corresponds to the situation where $\alpha = 1$ in qutrit and higher-dimensional cases, as shown in the light yellow area of Fig. 1(b). $R_2^{(d)}$ gives the bottom left corner, which can be derived from states with $\alpha < 1$.$R_1^{(d)}$ and $R_2^{(d)}$ together form the whole uncertainty region of $R^{(d)}$. When $\alpha = 0$, the region is reduced to the original point $(0, 0)$, which is intuitive since this state can never be projected into the qubit subspace, and the measurement outcomes of A, B are simultaneously determined. Compared to the qubit case, due to the unnormalization of $\rho^{(2)}$, the main difference of higher-dimensional system is that the bottom left corner can also be obtained. $R_1^{(d)}$ behaves as the same way as in the qubit case when θ changes while $R_2^{(d)}$ becomes larger as θ increases. When $\theta = \pi/4$, the lower left area is fully filled and when $\theta > \pi/4$, $R_2^{(d)}$ keeps getting larger, thus the UR covers the whole box.

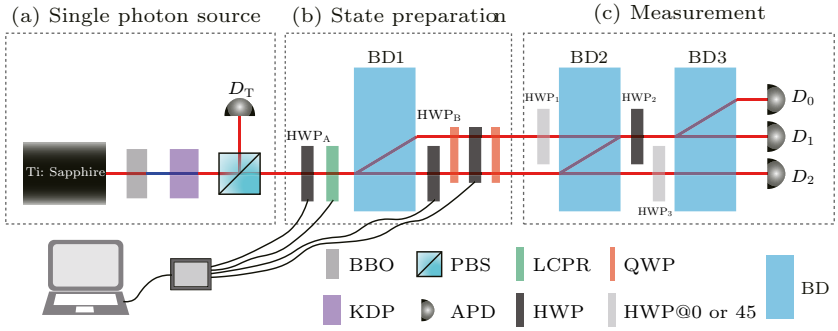

Fig. 2. Schematic picture of experimental setup. (a) Frequency-doubled Ti:sapphire laser pulses (∼150 fs duration, 415 nm) pump a phase-matched potassium di-hydrogen phosphate (KDP) crystal to generate photon pairs via spontaneous parametric down conversion. The photon pairs are then divided into signal and idler modes by a polarizing beamsplitter (PBS). Detection of one photon in the idler mode heralds a single photon in the signal mode. (b) The state preparation module is composed of two electronically controlled half-wave plates (HWPs), a liquid crystal phase retarder (LCPR), a birefringent calcite beam displacer (BD) and another electronically controlled HWP inserted in two quarter-wave plates (QWPs), which include a relative phase between horizontal and vertical polarization. (c) Three HWPs and two BDs project the single photon into three orthogonal states, then three avalanche photodiodes (APDs) are used for the detection of the single photon.

Experiment. We experimentally observe the qubit and qutrit uncertainty regions of different pairwise projective observables with photonic setups, as depicted in Fig. 2. This setup is designed to make the measurement of qutrit uncertainty regions compatible with the measurement of qubit ones. The qubit measurement outcomes can be obtained by blocking the third output port or post-selecting the qutrit measurement outcomes. According to Theorem 2, pure states and mixed states have the same uncertainty region for projective observables, therefore, in our experiment, we only deal with pure state systems. In the state preparation module, heralded single photons generated from single photon source module firstly are scrambled in the superposition of horizontal and vertical polarizations by the half-wave plate (HWP) $\mathrm{HWP_A}$, then a relative phase is introduced by the liquid crystal phase retarder (LCPR). After a birefringent calcite beam displacer (BD) and the $\mathrm{HWP_B}$, single photons are encoded in the su-

perposition of polarization and spatial optical modes. Another phase retarder is realized by two quarter-wave plates (QWPs) and an HWP, which constitute a QWP-HWP-QWP configuration and add a relative phase between horizontal and vertical polarizations. After that, an arbitrary pure qutrit state $|\psi\rangle = e^{i\phi_1}\cos\theta_A|0\rangle + e^{i\phi_2}\sin\theta_A\sin\theta_B|1\rangle - \sin\theta_A\cos\theta_B|2\rangle$ is generated [see the Supplemental Material, Section Ⅱ(A)]. We define the three eigen-modes of a qutrit state as

$$|0\rangle \equiv |s_1\rangle \otimes |H\rangle,\ |1\rangle \equiv |s_2\rangle \otimes |H\rangle,\ |2\rangle \equiv |s_2\rangle \otimes |V\rangle.$$

Here $|s_1\rangle, |s_2\rangle$ denote the spatial mode 1 (top) and spatial mode 2 (lower), $|H\rangle$ and $|V\rangle$ denote the horizontal and vertical polarization, respectively. By changing the setting angles of $\mathrm{HWP_A}$ and $\mathrm{HWP_B}$ and applying appropriate setting parameters to the two phase retarders, different pure qutrit states can be prepared.

In the measurement part, we use two BDs and three HWPs to implement a 3×3 unitary transformation on the input state, then three avalanche photodiodes (APDs) are used for the detection of the single photon, which are as a whole equivalently performing three orthogonal projective measurements on the input state.[42] Thus the three projectors have the same angle $\Theta = \frac{\pi}{2}$ between each other. To observe the UR of projectors with different Θ, we can change the wave-plate angles in the measurement module to implement different projective measurements. For example, in our experiment, by setting the angle of HWP3 to 0° and the angle of HWP2 to θ_2, the projective measurements realized in $\mathrm{D_0}$ port have the exact form of the second projector in Eq. (4) [see more details in the Supplemental Material, Section Ⅱ(B)]. That is,

$$P = \begin{pmatrix} \cos^2(2\theta_2) & \sin(2\theta_2)\cos(2\theta_2) & 0 \\ \sin(2\theta_2)\cos(2\theta_2) & \sin^2(2\theta_2) & 0 \\ 0 & 0 & 0 \end{pmatrix}, \tag{8}$$

with an angle $\Theta = 2\theta_2$ between the eigen-projector $|0\rangle\langle0|$. Then by changing the setting angle of HWP2 to θ_2', the resulting projector P' share $\Theta(P,P') = 2(\theta' - \theta)$ with P. Therefore, so long as inputting the same state into the measurement devices for enough trials and collecting the measurement statistics, the expectation values and variances of different projectors can be estimated. In order to observe the whole qutrit UR of a pair of projective measurements, enough different states need to be sampled. In this configuration, we can also realize the observation of qubit URs by simply blocking detector $\mathrm{D_2}$ or normalizing the detection events of detector $\mathrm{D_0}$ and $\mathrm{D_1}$.

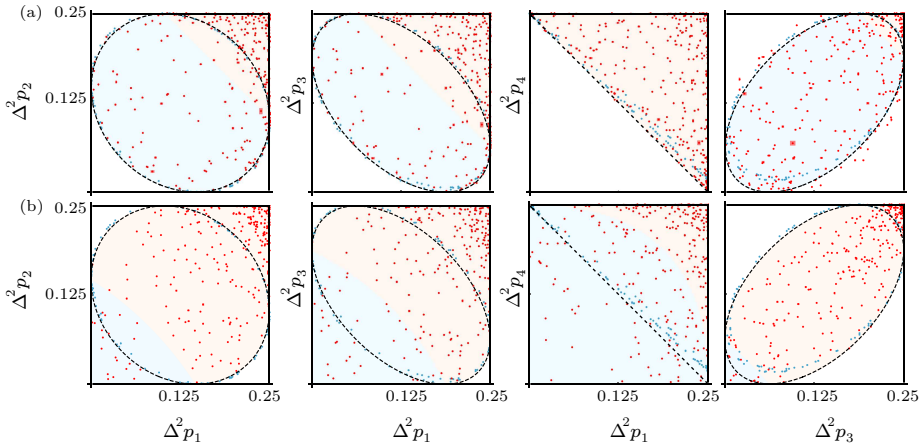

Fig. 3. Experimental observation of uncertainty regions (URs). Experimentally observed URs of a pair of (a) qubit and (b) qutrit projectors with $\Theta(j,k) = 5\pi/36, \pi/6, \pi/4, \pi/12$, respectively. R_1 and R_2 of theoretical URs are filled with light orange and light blue colors, respectively. Red points represent the first family of uniformly sampled 300 states, while blue points correspond to the 100 boundary states. Red and blue shaded areas correspond to the experimentally derived error bars. Most of the error bars are too small to observe. The theoretical ellipses given by the second inequality in Eq. (3) are plotted with black dashed curves.

The experiment is robust against state preparation errors, so long as enough states are sampled and these states are uniformly distributed, the shape of URs can be observed. Hence, we uniformly sampled two families of pure qutrit states. The first is 300 arbitrary pure qutrit states to give an overall observation of the UR. The other is the 100 boundary states with eigen-mode $|2\rangle$ fully unoccupied or termed as the real states (the phase between mode $|0\rangle$ and $|1\rangle$ is 0 or π), which lie on the boundary of the ellipse in Eqs. (3) and (6). By setting $\theta_2 = \{0, 5\pi/72, \pi/12, \pi/8\}$, four projective measurements on the total 400 states are realized in detector $\mathrm{D_0}$, with an angle $\Theta = 2\theta_2$ between the eigen-projector $|0\rangle\langle0|$. We denote the four projective measurement operators as P_1, P_2, P_3 and P_4, respectively. Together with detector $\mathrm{D_0}$, $\mathrm{D_1}$, detector $\mathrm{D_2}$ and the heralding detector $\mathrm{D_T}$, the statistics of measurement outcomes are registered by a coincidence logic with a coincidence window of 4.5 ns. From the measured statistics, the average values and

variances of the four projectors for 400 input states were calculated. Dividing the four projectors into four pairs of observables, $\{P_1, P_2\}$, $\{P_1, P_3\}$, $\{P_1, P_4\}$ and $\{P_3, P_4\}$, their experimental results are shown in Fig. 3(b). By post-selecting and normalizing the measured statistics in D_0 and D_1, we also derive the expectation values and variances of four qubit projectors, which is the nonzero two-dimensional block in P_j, denoted as $p_j (j = 1, 2, 3, 4)$. Their experimental results are shown in Fig. 3(a).

For each pair of projectors $P_j(p_j)$ and $P_k(p_k)$ written in the form of Eq. (8), the angle $\Theta(j, k)$ between them can be derived as $\Theta(j, k) = 2(\theta_{2k} - \theta_{2j})$. In Fig. 3, it can be seen that almost all the two families of states (red points for the first family and blue points for the boundary states) are within their theoretical regions and show agreement well with the theoretical predictions, for both qutrit and qubit experimental results. Particularly, most of the blue points fall in the neighboring of the dashed ellipses. The experimental results conclusively demonstrate our analytical characterization in the qubit and qutrit situation. Points out of the regions mainly attributed to instability of the interferometer during the whole measurement process, see the Supplemental Material, Section II(C) for a detailed analysis. The error bars plotted in Fig. 3 with shaded areas are quite small, because they mainly originate from statistical fluctuation, which become smaller when the photon count increases, also see Section II(C).

In summary, we have developed the notion of uncertainty region to geometrically characterize the entire area of variances of a set of observables. This region gives an entire description of the uncertainty relations of a pair of or more incompatible observables. Once the UR has been characterized, any other forms of variance-based uncertainty relations can also be determined. Furthermore, we point out that geometric features of URs may be used to quantify incompatibility of different observables. URs are also viewed as a kind of state-independent uncertainty relation, because it gives region for all quantum state (pure or mixed). Comparing to the previous works, we point out that UR is necessarily semialgebraic, for both pure states and mixed states. Further, by applying Jordan's Lemma, we give a complete analytical characterization of URs for a pair of qubit observables and a pair of arbitrary dimensional projective observables. Versatile photonic setups are used for observing URs of qubit and qutrit projectors and the results are highly consistent with the theory. Our work provides a new method for studying the uncertainty regions of incompatible observables and gives a new perspective for understanding and representing the uncertainty of quantum observables.

References

[1] Heisenberg W 1927 *Z. Phys.* **43** 172
[2] Gühne O 2004 *Phys. Rev. Lett.* **92** 117903
[3] Berta M, Christandl M, Colbeck R *et al.* 2010 *Nat. Phys.* **6** 659
[4] Li C F, Xu J S, Xu X Y *et al.* 2011 *Nat. Phys.* **7** 752
[5] Prevedel R, Hamel D R, Colbeck R *et al.* 2011 *Nat. Phys.* **7** 757
[6] Oppenheim J and Wehner S 2010 *Science* **330** 1072
[7] Kaniewski J M K, Tomamichel M and Wehner S 2014 *Phys. Rev. A* **90** 012332
[8] Busch P, Lahti P and Werner R F 2014 *Rev. Mod. Phys.* **86** 1261
[9] Coles P J, Berta M, Tomamichel M *et al.* 2017 *Rev. Mod. Phys.* **89** 015002
[10] Ozawa M 2003 *Phys. Rev. A* **67** 042105
[11] Busch P, Lahti P and Werner R F 2013 *Phys. Rev. Lett.* **111** 160405
[12] Buscemi F, Hall M J W, Ozawa M *et al.* 2014 *Phys. Rev. Lett.* **112** 050401
[13] Zhou F, Yan L, Gong S *et al.* 2016 *Sci. Adv.* **2** e1600578
[14] Kennard E H 1927 *Z. Phys.* **44** 326
[15] Weyl H 1927 *Z. Phys.* **46** 1
[16] Robertson H P 1929 *Phys. Rev.* **34** 163
[17] Schrödinger E 1930 *Proc. Prussian Acad. Sci.* **19** 296
[18] Maccone L and Pati A K 2014 *Phys. Rev. Lett.* **113** 260401
[19] Pati A and Sahu P 2007 *Phys. Lett. A* **367** 177
[20] Huang Y 2012 *Phys. Rev. A* **86** 024101
[21] Chen B and Fei S M 2015 *Sci. Rep.* **5** 14238
[22] Chen B, Cao N P, Fei S M *et al.* 2016 *Quantum Inf. Process.* **15** 3909
[23] Mondal D, Bagchi S and Pati A K 2017 *Phys. Rev. A* **95** 052117
[24] de Guise H, Maccone L, Sanders B C *et al.* 2018 *Phys. Rev. A* **98** 042121
[25] Hirschman I I 1957 *Am. J. Math.* **79** 152
[26] Beckner W 1975 *Ann. Math.* **102** 159
[27] Deutsch D 1983 *Phys. Rev. Lett.* **50** 631
[28] Maassen H and Uffink J B M 1988 *Phys. Rev. Lett.* **60** 1103
[29] Sánches-Ruiz J 1998 *Phys. Lett. A* **244** 189
[30] Coles P J and Piani M 2014 *Phys. Rev. A* **89** 022112
[31] Xiao Y, Jing N and Li-Jost X 2017 *Quantum Inf. Process.* **16** 104
[32] Demirel B, Sponar S, Abbott A A *et al.* 2019 *New J. Phys.* **21** 013038
[33] Abbott A A, Alzieu P L, Hall M J W *et al.* 2016 *Mathematics* **4** 1
[34] Schwonnek R, Dammeier L and Werner R F 2017 *Phys. Rev. Lett.* **119** 170404
[35] Sponar S, Danner A, Obigane K *et al.* 2020 *Phys. Rev. A* **102** 042204
[36] Zhao Y Y, Xiang G Y, Hu X M *et al.* 2019 *Phys. Rev. Lett.* **122** 220401
[37] Li J L and Qiao C F 2015 *Sci. Rep.* **5** 12708
[38] Abbott A, Alzieu P L, Hall M *et al.* 2016 *Mathematics* **4** 8
[39] Busch P and Reardon-Smith O 2019 arXiv:1901.03695v1 [quant-ph]
[40] Coste M 2002 *An Introduction to Semialgebraic Geometry* (Citeseer)
[41] Böttcher A and Spitkovsky I 2010 *Linear Algebra Its Appl.* **432** 1412
[42] Reck M, Zeilinger A, Bernstein H J *et al.* 1994 *Phys. Rev. Lett.* **73** 58

Supplementary Material for "Entirety of Quantum Uncertainty and Its Experimental Verification"

Jie Xie,[1,2,*] Li Zhou,[3,*] Aonan Zhang,[1,2] Huichao Xu,[1,2] Man-Hong Yung,[4,5] Ping Xu,[1,2,6] Nengkun Yu,[7,†] and Lijian Zhang[1,2,‡]

[1] *National Laboratory of Solid State Microstructures, College of Engineering and Applied Sciences and School of Physics, Nanjing University, Nanjing 210093, China*
[2] *Collaborative Innovation Center of Advanced Microstructures, Nanjing University, Nanjing 210093, China*
[3] *Department of Computer Science and Technology, Tsinghua University, Beijing, China*
[4] *Shenzhen Institute for Quantum Science and Engineering and Department of Physics, Southern University of Science and Technology, Shenzhen 518055, China*
[5] *Shenzhen Key Laboratory of Quantum Science and Engineering, Southern University of Science and Technology, Shenzhen 518055, China*
[6] *Institute for Quantum Information & State Key Laboratory of High Performance Computing, College of Computer, National University of Defense Technology, Changsha 410073, China*
[7] *Centre for Quantum Software and Information, School of Software, Faculty of Engineering and Information Technology, University of Technology Sydney NSW*

(Dated: June 17, 2021)

I. DETAILED THEORETICAL DERIVATION

A. Proof of Theorem 2

Let $A = P + iQ$. According to the famous Hausdorff-Toeplitz theorem [1], we have that the numerical range of A

$$W(A) = \{\langle\psi|A|\psi\rangle : |\psi\rangle \text{ is pure}\}$$

is convex and compact. In other words, it equals

$$W'(A) = \{\mathrm{Tr}(\rho A) : \rho \text{ ranges over all mixed states.}\}$$

Directly, we know that $R_m = R_p$ in this case.

However, when the number of projectors increase, this is not true generally. For example, considering the following four qubit states

$$|\psi_1\rangle = |0\rangle\,, |\psi_2\rangle = -\frac{1}{\sqrt{3}}|0\rangle + \sqrt{\frac{2}{3}}|1\rangle\,, |\psi_3\rangle = -\frac{1}{\sqrt{3}}|0\rangle + e^{i\frac{2\pi}{3}}\sqrt{\frac{2}{3}}|1\rangle\,, |\psi_4\rangle = -\frac{1}{\sqrt{3}}|0\rangle + e^{-i\frac{2\pi}{3}}\sqrt{\frac{2}{3}}|1\rangle$$

which form a regular tetrahedron on the Bloch ball. Uncertainty region of their corresponding projectors $(\Delta^2 P_{|\psi_1\rangle}, \Delta^2 P_{|\psi_2\rangle}, \Delta^2 P_{|\psi_3\rangle}, \Delta^2 P_{|\psi_4\rangle})$ no longer have the statement $R_m = R_p$. For the maximally mixed state $\rho = \frac{1}{2}I$, it generates the point $(1/4, 1/4, 1/4, 1/4)$ in R_m, while for arbitrary pure qubit states, no one can achieve this point. Because for all pure states, it must have that $\Delta^2 P_{|\psi_1\rangle} + \Delta^2 P_{|\psi_2\rangle} + \Delta^2 P_{|\psi_3\rangle} + \Delta^2 P_{|\psi_4\rangle}) = \frac{2}{3}$.

B. Proof of Theorem 3

Proof. Let us consider the one-dimensional Gaussian wave packet at time 0:

$$\psi(x,0) = \frac{1}{\sqrt{a\sqrt{\pi}}} e^{-\frac{x^2}{2a^2} + ik_0\frac{x}{a}}.$$

* These authors contributed equally to this work.
† nengkunyu@gmail.com
‡ lijian.zhang@nju.edu.cn

It is straightforward to check ψ is normalized. Solving the Schrödinger equation

$$i\hbar\frac{\partial}{\partial t}\psi(x,t) = \frac{p^2}{2m}\psi(x,t) = -\frac{\hbar^2}{2m}\frac{\partial^2}{\partial x^2}\psi(x,t)$$

with the initial condition $\psi(x,0)$ results that:

$$\psi(x,t) = \frac{1}{\sqrt{a\sqrt{\pi}}}\frac{1}{\sqrt{1+\frac{i\hbar}{ma^2}t}}e^{-\frac{1}{2}k_0^2}e^{-\frac{1}{1+\frac{i\hbar}{ma^2}t}\frac{1}{2}\left(\frac{x}{a}-ik_0\right)^2}.$$

After tedious calculations, we obtain the expectations of x, x^2, p, p^2:

$$\begin{aligned}
\langle x\rangle_{\psi(x,t)} &= \int_{-\infty}^{\infty}\psi(x,0)^*\psi(x,0)x\,\mathrm{d}x = \frac{\hbar k_0 t}{ma},\\
\langle x^2\rangle_{\psi(x,t)} &= \int_{-\infty}^{\infty}\psi(x,0)^*\psi(x,0)x^2\,\mathrm{d}x\\
&= \frac{a^2}{2}+\frac{\hbar^2t^2}{2m^2a^2}+\frac{\hbar^2k_0^2t^2}{m^2a^2},\\
\langle p\rangle_{\psi(x,t)} &= -i\hbar\int_{-\infty}^{\infty}\psi(x,0)^*\frac{\partial}{\partial x}\psi(x,0)\,\mathrm{d}x = \hbar\frac{k_0}{a},\\
\langle p^2\rangle_{\psi(x,t)} &= -\hbar^2\int_{-\infty}^{\infty}\psi(x,0)^*\frac{\partial^2}{\partial x^2}\psi(x,0)\,\mathrm{d}x\\
&= \hbar^2\frac{1}{2a^2}+\hbar^2\frac{k_0^2}{a^2}
\end{aligned}$$

which leads to:

$$\begin{aligned}
\Delta^2 x_{\psi(x,t)} &= \sqrt{\frac{a^2}{2}+\frac{\hbar^2t^2}{2m^2a^2}},\\
\Delta^2 p_{\psi(x,t)} &= \sqrt{\hbar^2\frac{1}{2a^2}}.
\end{aligned}$$

With proper choices of a and $t\geq 0$, $(\Delta^2 x_{\psi(x,t)}, \Delta^2 p_{\psi(x,t)})$ fulfills all regions of $S=\{(x,y): xy\geq\frac{\hbar}{2}, x,y>0\}$, or equivalently, $R_p = S$. Moreover, $R_p\subseteq R_m\subseteq S$ which implies $R_p = R_m = S$. □

C. Derivation of $R^{(2)}$

In the Bloch sphere representation, an arbitrary qubit density matrix ρ and two projectors A and B can be written as

$$\rho = \frac{1}{2}(I+\vec{r}\cdot\vec{\sigma}),$$

$$A = \frac{1}{2}(I+\vec{a}\cdot\vec{\sigma}),$$

$$B = \frac{1}{2}(I+\vec{b}\cdot\vec{\sigma}),$$

where $\vec{r}=(r_x,r_y,r_z), \vec{a}=(a_x,a_y,a_z), \vec{b}=(b_x,b_y,b_z)$ are unit Bloch vectors and $\vec{\sigma}=(\sigma_x,\sigma_y,\sigma_z)$ is the traceless Pauli operator vector. According to Lemma 1 in the main text, $\vec{a},\vec{b}$ can be written in the basis that $\vec{a}=(0,0,1)$ and $\vec{b}=(\sin 2\theta, 0, \cos 2\theta)$. Then by using the identity $(\vec{r}\cdot\vec{\sigma})(\vec{a}\cdot\vec{\sigma}) = (\vec{r}\cdot\vec{a})I + i(\vec{r}\times\vec{a})\cdot\vec{\sigma}$ and according to Born's rule, it can be derived that

$$\Delta^2 A = \frac{1}{4}\Big(1-(\vec{r}\cdot\vec{a})^2\Big),$$

$$\Delta^2 B = \frac{1}{4}\Big(1 - (\vec{r}\cdot\vec{b})^2\Big),$$

which can be further written as

$$r_x \sin 2\theta = \pm\sqrt{1 - 4\Delta^2 B} - r_z \cos 2\theta, \tag{S1}$$

$$r_z^2 = 1 - 4\Delta^2 A. \tag{S2}$$

The above two equations characterize the relationship between $\Delta^2 A$ and $\Delta^2 B$ for different Bloch vector $\vec{r}$. By ranging $\vec{r}$ over the whole Bloch ball, the set of $R_m^{(2)}$ can be fully characterized. From Eq.(S1) and Eq.(S2), it can be seen that the only constraint on $\vec{r}$ is $r_x^2 + r_z^2 \leq 1$, that is the positivity constraint. Embedding Eq.(S1) and Eq.(S2) into the constraint, $R^{(2)}$ can be derived from the following inequality

$$\pm 2\cos 2\theta\sqrt{(1 - 4\Delta^2 A)(1 - 4\Delta^2 B)} \leq 4(\Delta^2 A + \Delta^2 B) - (1 + \cos^2 2\theta), \tag{S3}$$

which is equivalent to the union set of the following two regions

$$R_1^{(2)} : \begin{cases} \Delta^2 A + \Delta^2 B \geq (1 + \cos^2 2\theta)/4, \\ \Delta^2 A, \Delta^2 B \leq 1/4, \end{cases} \tag{S4}$$

$$R_2^{(2)} : \begin{cases} \Delta^2 A + \Delta^2 B \leq (1 + \cos^2 2\theta)/4, \\ 16x_1^2/\cos^2(2\theta) + 16y_1^2/\sin^2(2\theta) \leq 1, \end{cases} \tag{S5}$$

where x_1 and y_1 are

$$\begin{pmatrix} x_1 \\ y_1 \end{pmatrix} = \sqrt{2}\begin{pmatrix} \cos\frac{\pi}{4} & \sin\frac{\pi}{4} \\ -\sin\frac{\pi}{4} & \cos\frac{\pi}{4} \end{pmatrix}\begin{pmatrix} \Delta^2 A - 1/8 \\ \Delta^2 B - 1/8 \end{pmatrix}.$$

The second inequality in $R_2^{(2)}$ characterize the ellipse plotted in Fig 1(a) in the main text. It is easy to check that when $r_x^2 + r_z^2 = 1$, Eq. (S3) also become an equation. So it is apparent that states with $r_y = 0$ constitute the boundary states of the ellipse, which is also called as "real states". In our experimental observation, we give a particular attention to these states.

D. Derivation of $R^{(d)}(d \geq 3)$

As shown in the main text, by applying Lemma 1, all the calculations in higher dimensional system can be reduced into the qubit subspace. The two rank 1 projectors A and B can be written as

$$A = \begin{pmatrix} 1 & 0 & & \\ 0 & 0 & & \\ & & \ddots & \end{pmatrix}, B = \begin{pmatrix} \cos^2\theta & \cos\theta\sin\theta & & \\ \cos\theta\sin\theta & \sin^2\theta & & \\ & & & \ddots \end{pmatrix},$$

in which the non-zero 2×2 blocks indicate the qubit subspace spaned by the two projectors. Thus the density matrix ρ can also be written in the same qubit subspace

$$\rho = \begin{pmatrix} \rho^{(2)} & & \\ & \ddots & \end{pmatrix},$$

where all the blank space set to 0 and $\rho^{(2)}$ is an unnormalized qubit density matrix

$$\rho^{(2)} = \frac{1}{2}(\alpha I + \vec{r}\cdot\vec{\sigma}),$$

satisfying $0 \leq \alpha \leq 1$ and $r^2 \leq \alpha^2$ as the positivity constraint. Here $\alpha = \mathrm{Tr}(\rho^{(2)})$ is the probability that ρ been projected into the qubit subspace. With the above representation, all the calculation can be reduced in the qubit subspace and it is easy to derive

$$\begin{aligned} \Delta^2 A &= \frac{1}{2}(\alpha + \vec{r}\cdot\vec{a}) - \frac{1}{4}(\alpha + \vec{r}\cdot\vec{a})^2 \\ \Delta^2 B &= \frac{1}{2}(\alpha + \vec{r}\cdot\vec{b}) - \frac{1}{4}(\alpha + \vec{r}\cdot\vec{b})^2. \end{aligned} \tag{S6}$$

Then we can solve the coordinates of $\vec{r}$ from Eq. (S6)

$$\begin{aligned} r_z &= 1-\alpha \pm \sqrt{1-4\Delta^2 A} \\ r_x &= \frac{1}{\sin 2\theta}[(1-\alpha - r_z\cos 2\theta) \pm \sqrt{1-4\Delta^2 B}]. \end{aligned} \tag{S7}$$

Similarly, put the above equations into the positivity constraint $r_x^2 + r_z^2 \leq \alpha^2$, we can arrive a quadratic inequality about α,

$$f_1(\Delta^2 A, \Delta^2 B, \theta)\alpha^2 + f_2(\Delta^2 A, \Delta^2 B, \theta)\alpha + f_3(\Delta^2 A, \Delta^2 B, \theta) \leq 0, \tag{S8}$$

where $f_1(\Delta^2 A, \Delta^2 B, \theta)$, $f_2(\Delta^2 A, \Delta^2 B, \theta)$ and $f_3(\Delta^2 A, \Delta^2 B, \theta)$ are functions of $\Delta^2 A$, $\Delta^2 B$ and θ. Given the fact that $0 \leq \alpha \leq 1$, if there exists an $\alpha \in [0,1]$ and corresponding parameters $(\Delta^2 A, \Delta^2 B, \theta)$ that Eq. (S8) can be satisfied, then the point $(\Delta^2 A, \Delta^2 B)$ is attainable, thus by discussing the above existing problem about inequality (S8) for all the combinations of signs in Eq. (S7), $R^{(d)}$ can be derived. Specifically, for example, when r_x and r_z in Eq. (S7) both take minus sign, we have

$$\begin{aligned} f_1 &= \tan^2\theta, \\ f_2 &= \sec^2\theta(\sqrt{1-4\Delta^2 A} + \sqrt{1-4\Delta^2 B} - 2), \\ f_3 &= -\frac{1}{\sin^2 2\theta}[2\cos 2\theta(\sqrt{1-4\Delta^2 A}-1)(\sqrt{1-4\Delta^2 B}-1) - (\sqrt{1-4\Delta^2 A}-1)^2 - (\sqrt{1-4\Delta^2 B}-1)^2]. \end{aligned}$$

By defining the quadratic function $F(\alpha) = f_1\alpha^2 + f_2\alpha + f_3$, which is symmetry with respect to the line $\alpha = \alpha_0 = -\frac{f_2}{2f_1}$ and get its minimum value at $(\alpha_0, \frac{4f_1 f_3 - f_2^2}{4f_1})$, the above existing problem can be satisfied in the following two situations,

$$\begin{cases} \alpha_0 \geq 1, \\ F(1) \leq 0 \end{cases}$$

$$\begin{cases} 0 \leq \alpha_0 \leq 1, \\ \frac{4f_1 f_3 - f_2^2}{4f_1} \leq 0 \end{cases}$$

The above two situations correspond to the two graphs in Fig. S1. Put the explicit form of f_1, f_2, f_3 into the above equation, we get the following two attainable regions of $(\Delta^2 A, \Delta^2 B)$

$$R_1^{(d)}: \begin{cases} 2 - \sqrt{1-4\Delta^2 A} - \sqrt{1-4\Delta^2 B} \geq 2\sin^2\theta, \\ \pm 2\cos 2\theta\sqrt{(1-4\Delta^2 A)(1-4\Delta^2 B)} \\ -4(\Delta^2 A + \Delta^2 B) + (1+\cos^2 2\theta) \leq 0, \end{cases} \tag{S9}$$

$$R_2^{(d)}: 2 - \sqrt{1-4\Delta^2 A} - \sqrt{1-4\Delta^2 B} \leq 2\sin^2\theta. \tag{S10}$$

Next, we consider the other 3 combinations of signs in Eq. (S7) and the union set of all the attainable regions equal to the uncertainty region $R^{(d)}$. However, it can be verified that the attainable regions in Eq. (S9) and Eq. (S10) cover the other three combinations and equal to $R^{(d)}$. Therefore, for higher dimensional quantum systems, their uncertainty regions of two projectors A, B are completely charecterized by Eq. (S9) and Eq. (S10).

II. EXPERIMENTAL DETAILS

A. Qutrit state preparation

We use a birefringent calcite beam displacer (BD), wave plates, a liquid crystal phase retarder (LCPR) and a half-wave plate sandwiched by two quarter-wave plates (QWPs) (a QWP-HWP-QWP configuration) to prepare arbitrary pure qutrit states in the form

$$|\psi\rangle = e^{i\phi_1}\cos\theta_A|0\rangle + e^{i\phi_2}\sin\theta_A\sin\theta_B|1\rangle - \sin\theta_A\cos\theta_B|2\rangle,$$

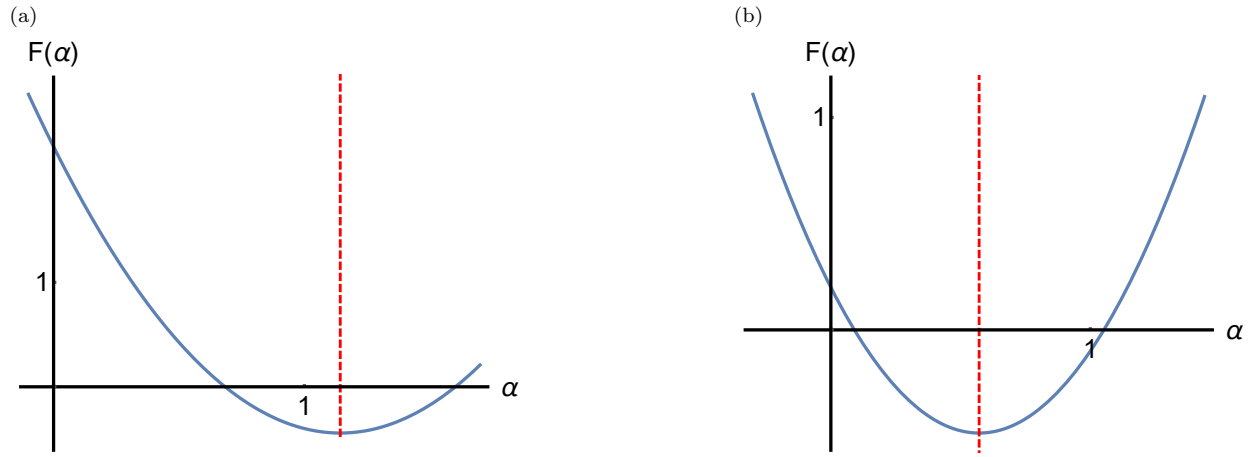

FIG. S1. Two exemplary pictures of of $F(\alpha)$. The blue curves are the images of $F(\alpha)$ that satisfy the above existing problem and therefore satisfy the positivity constraint. The red dashed lines are the symmetrical axes of $F(\alpha)$. (a) When $\alpha_0 \geq 1$, as long as $F(1) < 0$, Eq. (S8) can be satisfied. (b) When $\alpha_0 \in [0, 1)$, as long as the minimum value of $F(\alpha)$ less than 0, Eq. (S8) can be satisfied by some $(\Delta^2 A, \Delta^2 B)$ for a given θ.

which encoded in three product modes of the polarization and spatial modes, as clarified in the main text. The angle of $\mathrm{HWP_A}$ and $\mathrm{HWP_B}$ are set as θ_A and θ_B to distribute single photons among the three optical modes. The two phase factor ϕ_1 and ϕ_2 are implemented by the LCPR and the QWP-HWP-QWP configuration, respectively. The LCPR (Thorlabs, LCC1113-B) is set with its optical axis parallel to the horizontal polarization and add a relative phase ϕ_1 between horizontal and vertical polarization. Due to the tiny separating distance (4mm) of the two spatial modes and limited retardance uniformity of the liquid crystal phase retarder, we use a QWP-HWP-QWP configuration as the second phase retarder, with two QWPs setting at 45° and an electronically-controlled HWP setting at diferent angles, simultaneously manipulating the two spatial modes, to realize different ϕ_2. Detailed derivation of the state preparation procedure is given in Ref. [2], in which, the same method was used to prepare arbitrary pure qutrit states.

B. Measurement of uncertainty regions

As depicted in Fig. 2(c), by setting a appropriate angle θ_2 of HWP2, we implement three orthogonal qutrit projective measurements on the output ports of the measurement module. Therefore, HWP2 together with HWP3 perform the following unitary in the Jones matrix notation on the input state

$$U = \begin{pmatrix} \cos 2\theta_2 & \sin 2\theta_2 & 0 \\ \sin 2\theta_2 & -\cos 2\theta_2 & 0 \\ 0 & 0 & 1 \end{pmatrix},$$

which can be written in a more intuitive form

$$U = |0\rangle\langle\psi_0| + |1\rangle\langle\psi_1| + |2\rangle\langle\psi_2|, \tag{S11}$$

where $|\psi_0\rangle = \cos 2\theta_2|0\rangle + \sin 2\theta_2|1\rangle, |\psi_1 >= \sin 2\theta_2|0\rangle + \cos 2\theta_2|1\rangle$ and $|\psi_2\rangle = |2\rangle$. From Eq. (S11), it can be seen that U transform the input state from the basis of $|\psi_i\rangle (i = 0, 1, 2)$ into experimental basis, then after BD3, detector $\mathrm{D_0}$ equivalently perform the projective measurement $|\psi_0\rangle\langle\psi_0|$. By setting different angles $\theta_{2j} = \{0, 5\pi/72, \pi/12, \pi/8\}$, the corresponding projective measurements in dector $\mathrm{D_0}$ can be written as

$$P_j = \begin{pmatrix} \cos^2 2\theta_{2j} & \cos 2\theta_{2j} \sin 2\theta_{2j} & 0 \\ \cos 2\theta_{2j} \sin 2\theta_{2j} & \sin^2 2\theta_{2j} & 0 \\ 0 & 0 & 0 \end{pmatrix},$$

thus the Θ between P_j and $|0\rangle\langle 0|$ is $2\theta_j$. For different pair of $\{P_j, P_k\}$, $\Theta(j, k) = 2(\Theta_k - \Theta_j)$.

The above discussion shows how we implement different qutrit projective measurements. As for the qubit projectors, we only need to post-select and normalize the measured statistics of dector $\mathrm{D_0}$ and $\mathrm{D_1}$. Then different qubit projectors p_j is realized in dector $\mathrm{D_0}$, where p_j is the non-zero 2 by 2 block in P_j. By this method, we have measured URs of qubit and qutrit projective measurements simultaneously (in one experiment).

C. Experimental error analysis

For each sampled state, error bars of different observables plotted in Fig. 3 are derived from the four successively recorded photon counting statistics during each second. The total photon count is about $N = 45000$ for each second. Then, the standard derivations are calculated as error bars. The error bars in our experiments are originated from two aspects. One is the statistical fluctuation of photon counting statistics, which follows the multinomial distribution with the scaling $\sim \frac{1}{\sqrt{N}}$, and the other is the instability of experimental setup. Due to the stability of our laboratory environment in the time scaling of several seconds, the error bars in our experiment are mainly attributed to statistical fluctuations because they have the same scaling with statistical fluctuations, about 10^{-3} or less.

As mentioned in the main text, points generated by all states should be in its corresponding UR. Therefore, imperfection in the state preparation stage may lead to derivation between the experimental and theoretical value, but won't lead to experimental obtained points falling out of the theoretical region. As show in our experiment results, there exist several points out of the theoretical region in the fourth graph of Fig 3(a) in the main text. This is attributed to two aspects of experimental errors: systemic errors such as imperfection and inaccuracy of the wave-plates in the measurement module and instability of the interferometer formed by BD1 and BD2; the statistical fluctuation for finite trails. Consider that the errors in wave-plates are tiny (retardation errors, typically $\sim \lambda/300$ where $\lambda = 830$nm; setting angle errors ,typically ~ 0.2 degree; misalignment, typically ~ 0.1 degree) and the photon counting in our experiment is high (as mentioned above), the experimental errors are mainly caused by the slow drift and slight vibrating of the interferometer during the whole measurement progress (about 80 minutes for all 400 states), which lead to a limited interference visibility and thus biased projective measurement. However, during the whole measuring progress of $\{(\Delta^2 p_3, \Delta^2 p_4)\}$, the average interference visibility is above 98%. Except for the before mentioned several points in the fourth graph of Fig 3(a), almost all experimental datas are located in its corresponding theoretical regions.

[1] Hausdorff F, 1919. *Mathematische Zeitschrift* **3** 1 314.
[2] Xie J, Zhang A, Cao N *et al.*, 2020. *Phys. Rev. Lett.* **125** 150401.